

Voltage distribution studies ONZnO arresters

U. Kumar and V. Mogaveera

Abstract: The voltage distribution in a zinc oxide (ZnO) surge arrester under normal operating conditions has been observed to be non-uniform. The discs at the top are subjected to a higher voltage and hence thermal stresses; leading to a faster thermal ageing of these highly stressed discs. Therefore, efforts are generally made to make the voltage distribution as uniform as possible. The voltage distribution in the arrester is governed by the geometry as well as the electrical properties of the materials used. To improve the voltage distribution, some changes in geometry are relatively easier to implement. The authors employ a numerical field computation approach to ascertain the influence of the geometry of different components of the arrester on its voltage distribution. Practical geometries of a 220 kV and a 400 kV class arrester are considered under both clean and uniformly polluted conditions. Some optimum values for the geometry of the components are obtained.

1 Introduction

Zinc oxide (ZnO) surge arresters have been used extensively in high voltage power systems for providing protection to the insulation in power apparatus against dangerous overvoltages. The life of these arresters is dependent on their steady state performance. It has been observed in practice that the voltage distribution in the arrester is quite non-uniform. As a result, the discs at the top share a higher voltage and hence higher thermal stresses than the remaining discs. This leads to a faster thermal ageing of the discs at the top. To overcome this problem efforts are generally made to make the voltage distribution as uniform as possible. This calls for a study on voltage distribution.

The voltage distribution can be studied either experimentally or theoretically. Generally the theoretical approach is cost-effective and versatile. Different numerical methods such as the finite element method [1-4] and the charge simulation method [5] have been employed in the literature. The equivalent circuit approach was also attempted with various equivalent capacitances obtained using the field solution [1, 4]. Many workers have validated their theoretical results by conducting laboratory experiments on the actual arrester assembly [2, 3, 5]. This has provided further validity and strength to the field theoretical approach.

The voltage distribution in an arrester is obviously governed by the geometry of the different components and the electrical properties of the participating materials. Of these, implementing changes in geometry is preferred for obtaining a more uniform voltage distribution. The earlier works [1-5] were not concerned with the dependence of voltage distribution on the geometry of different components of the arrester. The present work aims to address this. Further, surface conduction arising from environmental pollution has not been considered in the earlier theoretical

studies on voltage distribution. The present work also attempts to partly address this issue for uniform axisymmetric pollution deposition.

The numerical solution of the associated quasi-static electric fields is carried out for the study and will be dealt with first.

2 Solution of the electric field

For the field solution, a surge arrester presents a semi-open geometry with a large aspect ratio. A boundary-based method called the surface charge simulation method (SCSM), also sometimes termed the boundary element method (BEM), is adopted for the field computation. Under clean environmental conditions, conduction is limited to only the varistor discs and the ratio of capacitive displacement current to conduction current will be large [6]. Consequently, the voltage distribution will be capacitive, i.e. fully governed by the dielectric permittivities of the participating media. However, with surface conduction arising from pollution deposition, the governing field distribution tends to be capacitive-resistive, and hence the corresponding field solution is needed. The details of the SCSM formulation for both clean and polluted conditions are given in the Appendix (Section 6).

As in earlier works, only one phase is considered for analysis. This makes the problem axisymmetric and hence only the solution of an axisymmetric field is sought.

For the verification of the methodology and code, the experimental results of Kojima *et al.* [5] were considered. The computed voltage distribution (with the geometry taken from their paper) is compared with their experimental data in Fig. 1. The maximum difference is only 6%, thus validating the numerical solution methodology.

3 Voltage distribution studies

3.1 Influence of the geometry of the components on the voltage distribution

The practical geometries of 220 kV and 400 kV class arresters are considered. Fig. 2 gives the cross-sectional details of the container along with the major dimensions. The total heights of these 220 kV and 400 kV arresters are

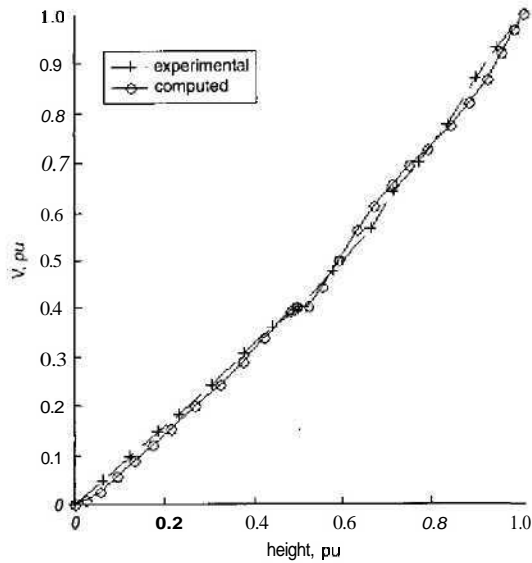


Fig. 1 Comparison of the computed voltage distribution with the measurements reported in [5]

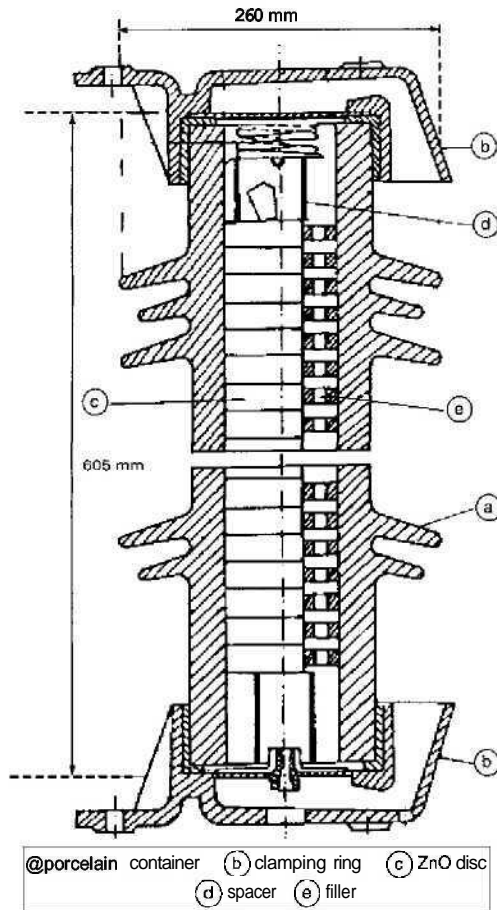


Fig. 2 Cross-sectional details of the container

2.66m and 3.79 m, respectively. Unless otherwise stated the simulations are carried out for arresters with 6 kV discs.

3.1.1 Influence of the grading ring (toroid) position: The grading ring is employed to make the

voltage distribution uniform. Its efficacy is clearly dependent on its relative position. The voltage distributions are therefore computed for different ring heights (H_{ring}). Some of the results obtained are plotted in Figs. 3 and 4 for 220kV and 400kV class surge arresters, respectively. In each of these Figures, the X-axis is the normalised height from the bottom. In these plots, the voltage can be seen to remain constant along the spacers and flanges of the containers. These Figures clearly demonstrate that the voltage drops very sharply near the line end in all cases. As a result, the corresponding gradients, as reported in the literature, are higher than the average value for the discs in the **top portion**, and lower than the average value for the discs in the remaining portions. Table 1 gives the maximum voltage gradient at different grading ring positions for both 220 kV and 400 kV arresters. It indicates that an optimum position for the ring ranges between 75 and 86% of the total

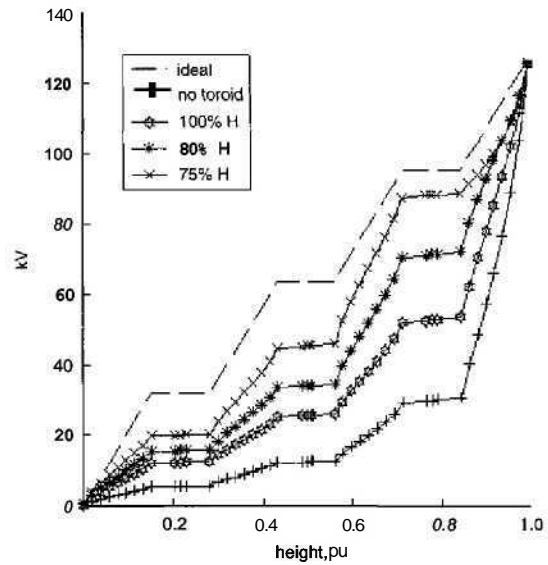


Fig. 3 Voltage distribution in 220kV arrester for various ring positions

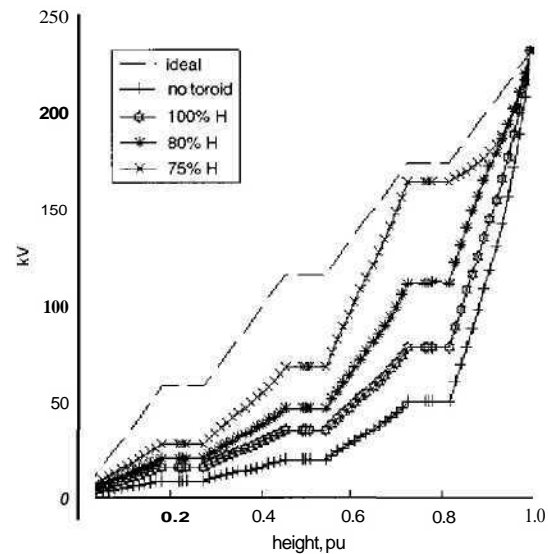


Fig. 4 Voltage distribution in 400kV arrester for various ring positions

Table 1: Maximum voltage gradient for different toroid positions

$\% (H_{ring} / H_{arrester})$	$\% (E_{max} / E_{avg})$ 220 kV arrester	$\% (E_{max} / E_{avg})$ 400 kV arrester
No toroid	452.5	521.0
100	293.5	369.2
92	234.7	285.2
86	204.0	257.9
80	200.0	264.0
75	211.6	276.1
70	232.3	304.9

arrester height. However, in reality, due to the increase in conductivity of the discs with the voltage gradient, the actual maximum stress can be less than these values. Nevertheless, the optimum height obtained from the studies would remain unaltered.

The variation of maximum gradient with ring position can be explained as follows. The electrostatic coupling between the stack and the ground causes a nonlinear distribution of the voltage. When the ring is present it provides additional electrostatic coupling to the stack from the source, which will partly compensate for the coupling to the ground and as a consequence the voltage distribution improves. When the height of the ring is the same or greater than the stack height, the coupling provided by the ring to the top portion of the stack is more than that to the bottom portion of the stack. However, the voltage difference between the top portion discs and the ring is less, when compared to the bottom portion discs, lessening the improvement in the voltage distribution. As the ring height is lowered, the coupling to the bottom portion improves and the voltage at the bottom portion increases; consequently the voltage gradient at the top portion decreases. After an optimum point, further lowering of the ring results in increased coupling to the middle and bottom portions and the maximum gradient point shifts towards the middle. Consequently, the magnitude of the maximum gradient starts to increase.

3.1.2 Influence of cross-section of the toroid:

The coupling provided by the ring is obviously dependent on the cross-section. To ascertain this, the cross-sectional radius of the ring was varied and the voltage distribution was computed with the ring kept at the same optimum height. Table 2 gives the computed maximum gradients. It seems to be very advantageous to have a ring with a larger cross-sectional radius for minimising the maximum gradient to which varistor elements are subjected.

The major radius of the ring is not vained as it can affect the clearance requirement between different phases.

Table 2: Maximum voltage gradient for different toroid c/s

dis diameter of toroid, mm	$\% (E_{max} / E_{avg})$ 220 kV arrester	$\% (E_{max} / E_{avg})$ 400 kV arrester
40	222.4	281.8
60	200.0	257.9
100	165.8	221.3

3.1.3 Effect of spacers: The voltage rating of the arrester depends on both the earth coefficient factor and the line-to-line voltage of the power system. The height of the porcelain housing is dependent on the voltage rating of the arrester and the environmental pollution conditions.

Thus, for a given voltage rating, the total height of the discs will be less than the height of the housing and hence metallic spacers are employed to make up the extra height. These spacers can form up to 40% of the arrester height. To ascertain the effect of these spacers, two cases were considered: arresters with 6 kV discs and arresters with 3 kV discs. The total heights of the discs with 6 kV discs are approximately 1.44m and 2.52m for 220 kV and 400 kV classes, respectively. The corresponding values with 3 kV varistors are 1.86m and 3.25m, respectively. Therefore, with 3 kV discs, spacer requirements are less than with 6 kV discs. The computed gradients are given in Table 3. It is clear from the Table that the lower the spacer height the better is the voltage distribution. This is because the presence of the spacers increases the average voltage per unit length along the arrester and hence the current to stray couplings to ground, thus making the voltage distribution more non-uniform.

Table 3: Maximum gradient with 3kV and 6kV discs

Voltage rating of disc, kV	$\% (E_{max} / E_{avg})$ 220 kV arrester	$\% (E_{max} / E_{avg})$ 400 kV arrester
3	180.3	233.1
6	200.0	257.9

Spacers in general can be placed either at the top or at the bottom, or equally divided between the top and bottom of each container. As spacers are inevitable, studies were undertaken to check for a better placement of these spacers, which possibly can give a lower maximum stress. The ring was kept at 80% height for both of the arresters. The computed voltage gradients from the study are given in Table 4.

Table 4: Maximum gradient for different spacer positions

Spacer position	$\% (E_{max} / E_{avg})$ 220 kV arrester	$\% (E_{max} / E_{avg})$ 400 kV arrester
Bottom	174.5	225.5
Equal (top and bottom)	189.2	230.4
Top	200.0	264.0

From the Table, it is evident that placing the spacer at the bottom of the container gives a minimum gradient. With this arrangement, the coupling provided by the grading ring to the discs is greater, compared to other spacer positions, and the average voltage along the arrester is relatively smaller. Therefore, there is a better voltage distribution, which results in a corresponding reduction in the maximum stress.

With the larger diameter discs, the displacement current through the discs becomes much stronger than that to stray couplings to the ground. As a consequence, the voltage distribution is found to improve. An increase in diameter of the porcelain container and a moderate variation in the base height of the stack are found to have insignificant influence on voltage distribution.

3.2 Voltage distribution studies under polluted conditions

The pollution severity depends on the environmental conditions in the location where the surge arresters are employed. Owing to various wetting processes, the pollution deposition on the porcelain container attains some conductivity. The higher the pollution levels, the higher the surface conductivity, and therefore the better the voltage distribution must be (if uniform deposition is assumed). Three levels are considered for the study, assuming uniform deposition: relatively dry deposition (surface conductivity = 1.0 nS), a low pollution level (68 nS) and a medium pollution level (10⁴ nS) [7].

The computed voltage distributions for three different conductivities are shown in Figs. 5 and 6. Table 5 gives corresponding maximum voltage gradients. In the computations, the toroid was held at the optimum position obtained for clean conditions and uniform deposition was assumed. It is evident from the Table that the surface conduction due to a medium level of pollution is sufficient to nullify the effect of electrostatic couplings to the ground. In other words, current through the pollution layer becomes much stronger than that into electrostatic couplings to the ground.

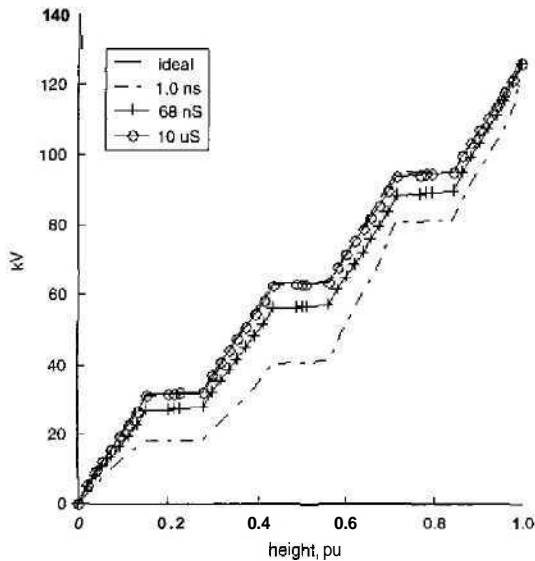


Fig. 5 Voltage distribution in 220 kV arrester under various pollution levels

Computations indicate that the effects of ring position and its cross-sectional diameter, and of spacer dimensions; are similar to those with clean conditions. However, with pollution the maximum gradients are lower than for clean conditions. Only uniform pollution is considered here.

4 Summary and Conclusions

It is important to make the voltage distribution in the ZnO arresters as uniform as possible. The voltage distribution is dependent on the geometry as well as the electrical properties of the materials of the surge arrester assembly. Some changes of geometry can be attempted to improve the voltage distribution. A study has been made of the influence of the geometry of different components of the arrester on its voltage distribution (under normal operating conditions),

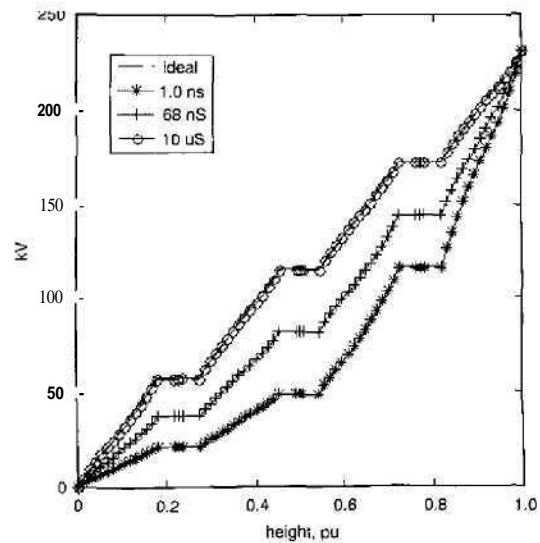


Fig. 6 Voltage distribution in 400 kV arrester under various pollution levels

Table 5 Maximum voltage gradient for different pollution levels

Surface conductivity nS (pollution level)	% (E_{max}/E_{avg}) 220 kV arrester	% (E_{max}/E_{avg}) 400 kV arrester level)
1.0 (dry)	199.7	256.1
68 (low)	130.1	192.5
10 ⁴ (medium)	100.0	100.0

Both clean and uniformly polluted conditions were considered.

For clean conditions, the maximum gradient for all cases occurs at the top. There is an optimum height for the grading ring ranging between 75 and 86% of the stack height at which this maximum gradient falls to a minimum. An increase in the cross-sectional diameter of the ring aids in reducing the maximum gradient.

The metallic spacers, which become necessary to make up the total height? arc found to cause an increase in the maximum gradient. With 3 kV discs; the spacer requirement is lesser and hence the maximum gradient is lower. Placing spacers at the bottom of each container is found to give a minimum stress, compared to spacers placed at the top and equally distributed between top and bottom. Both the base height and the diameter of the container are found to have an insignificant influence on the voltage distribution for the possible variation range.

Under uniformly polluted conditions, the voltage distribution remains non-uniform only for low pollution levels and relatively dry conditions. The influence of height and cross-sectional diameter of the ring, and height of the spacer; is found to be similar to that under clean conditions.

In conclusion, the present work has studied the influence of the geometry of different components of both 200 kV and 400 kV class outdoor ZnO surge arresters on their voltage distribution. Both clean and uniformly polluted conditions have been considered; and some optimum values for the geometry have been deduced.

5 References

- 1 CSENDES, Z.J. and HAMAN, J.R.: 'Surge arrester voltage distribution analysis by the Finite Element Method'. *IEEE Trans. Power Appar. Syst.*, 1981, **100**, (4), pp. 1806-1812
- 2 OYAM, M., OHSHIMA, I., HONDA, M., YAMASHITA, M., and KOJIMA, S.: 'Analytical and experimental approach to the voltage distribution on gapless Zinc-Oxide surge arresters'. *IEEE Trans. Power Appar. Syst.*, 1981, **100**, (11), pp. 4621-4627
- 3 ZHOU, P., and WANG, G.: 'Analysis of the potential distribution of gapless surge arrester'. VI International Symposium on High Voltage Engineering, 28 Aug.-1 Sept. 1989, New Orleans, LA, USA, pp. 1-4
- 4 HADDAD, A., and NAYLOR, P.: 'Finite-element computation of capacitance networks in multiple-electrode system: application to ZnO surge arresters'. *IEE Proc. Sci., Meas. Technol.*, 1998, **145**, (4), pp. 129-135
- 5 KOJIMA, S., OYAM, M., and YAMASHITA, M.: 'Potential distribution of metal oxide surge arresters under various environmental conditions'. *IEEE Trans. Power Deliv.*, 1988, **3**, (3), pp. 984-989
- 6 HIALEK, T.: 'Insulation system protection with zinc oxide surge arresters'. *IEEE Ektr. Insul. Mag.*, Jan./Feb 1999, **15**, (1), pp. 5-10
- 7 GOPAL, H.G.: 'An Electrothermal model for pollution induced flashover of insulators'. Ph.D. Thesis, Indian Institute of Science, Department of HVE, Bangalore, (India) May 1998
- 8 ERIC H.A. and PETER L.L.: 'Two dimensional and Axi-symmetric Boundary value problems in Electrostatics'. (Computational Fields Laboratory, Department of Electrical and Computer Engineering, Worcester Polytechnic Institute, Worcester, MA, USA 01609).
- 9 KIJMAR, U., and NAGABHUSHANA, G.R.: 'Capacitive-Resistive transients in terms of field quantities'. *J. Indian Inst. Sci.*, Sept.-Oct., 1994, **74**, pp. 633-645
- 10 CHAKRAVORTI, S., and STEINHIGLEK, H.: 'Boundary Element studies on insulator shape and electric field around HV insulators with or without pollution'. *IEEE Trans. Dielectr. Elcar. Insul.* 2000, **7**, (2), pp. 169-176

6 Appendix: Details of the field computation method

The surface charge simulation method (SCSM) employed in the present work is adopted from [8]. In an electrostatic field the applied excitation induces real charges on the conductor surface and apparent (polarisation) charges in dielectrics. The resulting field distribution is equivalent to that produced by surface charge distributions on the conductor boundaries and fictitious charge distributions at the dielectric interface with dielectrics replaced by vacuum. The SCSM attempts to simulate these real and fictitious charges by piecewise-defined surface charge distributions. As a consequence, the solution will satisfy the governing differential equation exactly, but satisfies the boundary conditions only approximately. The present work employs segments with a linearly varying charge distribution for the discretisation and Galerkin's method for deriving the SCSM equations.

6.1 Potential and field due to an axi-symmetric strip

6.1.1 Potential due to axi-symmetric strip: The potential at (r, z) due to an axi-symmetric strip with respect to infinity [8] is given by

$$V(r, z) = \frac{1}{4\pi\epsilon_0} \int \frac{\rho_s r' F^*(r', z') dl}{r^2}$$

where L is the length of the segment, dl is an elemental length on the segment, ϵ_0 is the permittivity of free space, ρ_s is the linear surface charge density, (r, z) are the coordinates of the measuring point, (r', z') is a point on the source segment and $dl = \frac{L}{T} dt$. The function F^* is given by

$$F^*(r', z') = \frac{4K(m)}{(a+b)^{1/2}}$$

where $a = r^2 + r'^2 + (z - z')^2$, $b = 2rr'$ and $K(m)$ is the elliptical integral of the first kind.

The linearly varying surface charge density along with the coordinates (r', z') can be expressed in terms of a normalised variable t as

$$\begin{aligned} \rho_s &= \left(\frac{\rho_{s2} - \rho_{s1}}{2} \right) t + \left(\frac{\rho_{s1} + \rho_{s2}}{2} \right); \\ r' &= \left(\frac{r_2 - r_1}{2} \right) t + \left(\frac{r_1 + r_2}{2} \right); \\ z' &= \left(\frac{z_2 - z_1}{2} \right) t + \left(\frac{z_1 + z_2}{2} \right) \end{aligned}$$

where $-1 \leq t \leq +1$ and (r_1, z_1) and (r_2, z_2) are the coordinates of the end points of the strip. The direct analytical integration of the above equation is impractical and hence Gaussian quadrature is employed. Calculation of the potential on the segment itself leads to a singularity and hence ordinary numerical integration fails. To overcome this problem, a direct integration on the simplified expression is adopted for the neighbourhood of the singularity and regular numerical integration for the remaining portion [8]. For the singularity on the starting point of the segment, the potential is given by

$$\begin{aligned} V(r_1, z_1) &\cong \frac{L}{2\pi\epsilon_0} \left[\rho_{s1} T \left(\ln \left(\frac{8r_1}{TL} \right) + 1 \right) \right. \\ &\quad \left. + (\rho_{s2} - \rho_{s1}) \frac{T^2}{2} \left(\ln \left(\frac{8r_1}{TL} \right) + \frac{1}{2} \right) \right] + \frac{L}{4\pi\epsilon_0} \\ &\quad \times \int_T^1 \frac{4\rho_s(r_1 + (r_2 - r_1)t)K(m)}{\sqrt{(2r_1 + (r_2 - r_1)t)^2 + ((z_2 - z_1)t)^2}} dt \end{aligned} \quad (2)$$

where

$$T = \frac{2r_1 \left(r_2 - r_1 + \sqrt{(r_2 - r_1)^2 + AL^2} \right)}{AL^2}$$

and A is taken as 99,

$$m = \frac{4r_1(r_1 + (r_2 - r_1)t)}{(2r_1 + (r_2 - r_1)t)^2 + ((z_2 - z_1)t)^2}$$

T is the value of t until that range potential is computed analytically and the rest is computed numerically. If T covers the whole range, then the potential is computed analytically.

For a singularity at another portion of the segment, the original segment is suitably divided near the singularity and each part is handled separately.

6.1.2 Electric field due to axi-symmetric

Strip: On similar lines, the electric field at any point (r, z) due to an axi-symmetric strip charge is given by [8]

$$E(r, z) = \frac{1}{4\pi\epsilon_0} \int \frac{\rho_s r' H^*(r', z') dl}{r^2}$$

where

$$\begin{aligned} H^*(r', z') &= \frac{2}{r(a+b)^{1/2}} \\ &\quad \times \left[K(m) - \frac{r'^2 - r^2 + (z - z')^2}{a - b} E(m) \right] \hat{a}_r \\ &\quad + \left[\frac{4(z - z')}{(a - b)(a + b)^{1/2}} E(m) \right] \hat{a}_z \end{aligned}$$

and $E(m)$ is the elliptical integral of the second kind.

The nonnal component of the field on the segment itself is computed directly by $E_n = \rho_s / 2\epsilon_0$.

6.2 SCSM formulation

For a segment on the Dirichlet boundary with a specified potential V_b , the Galerkin approach of minimising the residue leads to

$$\int_{\Gamma_i} N_k \sum_{i=1}^N \int_{\Gamma_j} \rho_s' F^*(r', z') dl' dl = 4\pi\epsilon_0 \int_{\Gamma_i} N_k V_b dl \quad (4)$$

where dl is the elemental length on the measuring segment. dl' is that on the source segment, N is the number of segments (strips). Γ_i is the cross-section of the source segment i and Γ_j is the cross section of the measuring strip j . There are two interpolation functions for each strip. $N_1 = (1-t)/2$, $N_2 = (1+t)/2$, and therefore k assumes 1 to 2.

Similarly, for a segment on the dielectric interface, the Galerkin approach to satisfying continuity of normal electric flux leads to

$$\int_{\Gamma_j} N_k \sum_{i=1}^N \left[\frac{\rho_{sf}}{2} + \epsilon_0 \frac{(\epsilon_1 - \epsilon_2) E_n}{(\epsilon_1 + \epsilon_2)} \right] dl = 0 \quad (5)$$

where ϵ_1 , ϵ_2 are permittivities of the media, ρ_{sf} is the fictitious charge on the interface and E_n is the normal component of the computed electric field at the interface segment due to the charges contained in other segments.

For the floating conductors, their potential V_j is unknown and therefore an additional variable appears in the formulation. However, by employing the equi-potentiality condition along with the condition on total charge; the above problem can be resolved. The final equations are

$$\int_{\Gamma_j} N_k \sum_{i=1}^N \int_{\Gamma_i} \rho_s' F^*(r', z') dl' dl = 4\pi\epsilon_0 \int_{\Gamma_j} N_k V_j dl \quad (6)$$

The above equation is applicable to all segments on a given floating conductor. For every floating conductor, the additional equation from the condition on charge is

$$\sum_{i=1}^N 2\pi \int \rho_s' dl - \sum_{i=1}^N Q_s = 0$$

where the last term represents the real charge, if any, on the floating conductors.

6.3 Modelling of surface conduction

The surface conduction originating from the deposition of the pollution at the air/porcelain interface can lead to the accumulation of charges along the interface.

At the material interface the electric field has to satisfy the condition $D_{1n} - D_{2n} = \sigma_s$, where σ_s is the **interfacial** surface charge density. Further, at the interface, any divergence in surface current densities must be compensated by the **displacement current** densities [9]: $\nabla_s \cdot J_s = -\partial\sigma_s/\partial t$, where J_s is the surface current density and $\nabla_s \cdot$ the divergence operator defined over the surface representing the interface.

From the above equation, the following equation can be arrived at [9, 10]:

$$j \left[\frac{V_{i-1} - V_i}{R_i} - \frac{V_i - V_{i+1}}{R_{i+1}} \right]$$

where $j = \sqrt{-1}$, ω is the angular frequency of the system voltage, $i-1$, $i+1$ denote grid points (ordered from the top), R_i and R_{i+1} are the surface resistances attributed to the segments under consideration, V_{i-1} , V_i , V_{i+1} are the potentials at the grid points and S_i is the surface area attributed to the grid point under consideration. The surface area and resistance can be computed by $S_i = l\pi(r_1+r_2)/2$, where l denotes the length of the segment; r_1 , r_2 are the radii of the end points of the segment and

$$R_i = \frac{k_s l}{2\pi(r_2 - r_1)} \log\left(\frac{r_2}{r_1}\right)$$

where k_s denotes the surface resistivity of the segment. When the two radii are equal then the surface resistance is given by $R_i = k_s l / 2\pi r_2$.

The corresponding BEM equation for the interface with surface conduction and hence the surface charge accumulation is

$$\int_{\Gamma_i} N_k \left[\rho_{si} f_{ii} + \epsilon_0 \frac{(\epsilon_1 - \epsilon_2)}{(\epsilon_1 + \epsilon_2)} \sum_{j=1, j \neq i}^N \rho_{sj} f_{ij} \right] dl - \left(\frac{1}{\epsilon_1 + \epsilon_2} \right) \frac{j}{\omega S_i} \int_{\Gamma_i} N_k \sum_{j=1}^N \rho_{sj} \left[p_{i-1, j} \frac{1}{R_i} - p_{i, j} \left(\frac{1}{R_i} + \frac{1}{R_{i+1}} \right) - p_{i+1, j} \frac{1}{R_{i+1}} \right] = 0 \quad (9)$$

where f_{ii} and f_{ij} are the self and mutual field coefficients, $p_{i-1, j}$, $p_{i, j}$ and $p_{i+1, j}$ are the potential coefficients of the nodes $i-1$, i if 1 with respect to segment of charge j , ρ_s is the surface charge density, ϵ_1 and ϵ_2 are the permittivities of the participating media, Γ_i is the cross-section of the segment i and N_k is the interpolation function.